

Detecting small low emission radiating sources

Moritz Allmaras ¹, David P. Darrow ³, Yulia Hristova ²,
Guido Kanschat ¹, and Peter Kuchment ¹

¹ Mathematics Department, Texas A&M University, College Station, TX

² Institute for Mathematics and its Applications, Minneapolis, MN

³ University of Texas Medical Branch, Galveston, TX

May 16, 2022

Abstract

The article addresses the possibility of robust detection of geometrically small, low emission sources on a significantly stronger background. This problem is important for homeland security. A technique of detecting such sources using Compton type cameras is developed, which is shown on numerical examples to have high sensitivity and specificity and also allows to assign confidence probabilities of the detection. *2D* case is considered in detail.

1 Introduction

One of the missions of the Department of Homeland Security is to prevent smuggling of weapon-grade nuclear materials (e.g., [24]). It is expected that such materials, unlike those needed for a "dirty bomb", will have low emission rates and will be well shielded, so that very few gamma photons or neutrons would escape, and even less would be detected non-scattered (ballistic). An additional hurdle for the detection of illicit nuclear substances is the strong natural radiation background. If the particles radiated by the source were distinct (e.g., in terms of their energies) from the ones prevalent in the background, then the detection would be easy. We thus assume that the particles from the source are identical to those coming from the background in terms of their nature, energies, etc., so the discrimination using such parameters is impossible. This leads to the situation when the signal to noise ratio (SNR), i.e. the count of the detected non-scattered particles emitted by the source versus the total number of detected particles, can be as low as 10^{-3} , if not lower. It is rather clear that if only the locations of the hits are detected, but no information about the directions of the incoming particles is available, there is no chance to detect the presence of such a weak source. Thus, one needs to employ detectors that can provide some directional information of the incoming particles. For instance, the γ -cameras most commonly used in SPECT (Single Photon Emission Computed Tomography) medical imaging [26], are mechanically collimated, and thus they "count" the particles coming from a narrow cone of directions (in the first approximation, just one direction) and discard the rest.

However, mechanical collimation dramatically reduces the particle count, and thus, for an extremely low emission source, can essentially completely eliminate the useful signal (this difficulty, although in much less extreme form, arises also in SPECT). Typically, only one out of thousands emitted photons is detected by a collimated camera. When dealing with low emission sources, one wants to capture as many emitted particles as possible, and thus mechanical collimation is unsuitable for the problem at hand.

Another option is to use the so called **Compton γ -cameras**, which do not discard any incoming particles by collimation. The price one pays for this is that the directional information provided by such a camera is more limited. Namely, one obtains just a hollow (i.e., surface) cone of possible directions rather than a single direction. Still, Compton cameras are good candidates for the applications we have in mind. While Compton cameras are available for detecting γ -photons, neutron detectors that provide a similar “incoming cone” information are being currently developed as well [24, 39]. The methods we will develop are not dependent upon a specific kind of particles; we will thus call all detectors that can provide the cone information **Compton type detectors**.

Even if directional information is available, the task of detecting the extremely low emission coming from a geometrically large source in the presence of a large background would be very hard, if not impossible. So, another important condition that we impose, besides availability of directional information, is the small size of the possible source, which is usually a safe assumption in the applications we are interested in.

Simulations of radiation from a small high-enriched uranium source placed in a cargo container suggest that only about 0.1% of the signal received by detectors might be due to the ballistic (non-scattered) particles emitted from the source. The remaining 99.9% of detected particles come either from extraneous (natural) sources, or from scattered source particles from the source [4].

One can try to use the rather standard emission tomography techniques in the present situation, albeit the chances of success (and even the applicability of the tomographic models) are questionable. This circle of issues is discussed analytically and tested numerically in Section 2, where the conclusion is made that backprojection technique might be the best bet here, while the usual filtration parts do not do any good. This conclusion gets its foundation in the probabilistic considerations of Section 3 and then in numerical examples of Section 4. However, all these considerations dealt with the simplest, collimated detectors, to check the viability of the approach. Section 5 is devoted to the case of Compton type cameras. Here tomographic and backprojection techniques are considered. The analysis of the 2D Compton camera case is discussed in Section 6. The corresponding numerical tests are conducted and discussed in Section 7. The overall conclusion is that the suggested backprojection Compton type cameras techniques allow a robust detection of presence of geometrically small low emission sources with extremely low SNR, with confidence levels attached.

The paper ends with the sections devoted to remarks and conclusions, acknowledgments, and bibliography.

2 Source detection using standard tomographic techniques

We will briefly present here some relevant mathematical formulas and conclusions from the SPECT version of emission tomography, which is the closest to the problem of our interest. One can find more details in [20, 21, 26, 27].

Let $f(x)$ be the intensity distribution of the sources of particles of certain type (γ -photons, neutrons, etc.) inside an object (e.g., cargo container, or a truck). Let also $\mu(x)$ be the distribution of the attenuation (also not known in our situation of an unknown cargo). Then, in the approximation of sufficiently high emission rate, the radiation transport equation implies that the count at a detector collimated in the direction L is

$$T_\mu f(L) = \int_L f(x) e^{-\int_{L_x} \mu(y) dy} dx. \quad (1)$$

Here L_x is the segment of the line L between the emission point x and the detector and dy denotes the standard linear measure on L . We will fix an origin O and assign

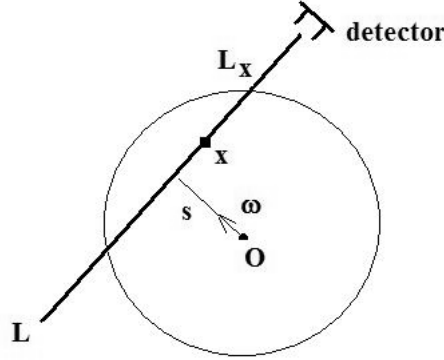


Figure 1: The set-up of the SPECT emission tomography

the normal coordinates (ω, s) to any line L . Here ω is an unit vector orthogonal to L and s is the (signed) distance from the origin to L (see Fig. 1). The equation of this line is $x \cdot \omega = s$ and the line itself will be sometimes denoted as $L_{(\omega, s)}$. The value of (1) provides the mathematical expectation of the counts at a detector per unit of time, which is not a good approximation of the measured data, if the emission rate is low. Let us still accept temporarily this integral-geometric formulation and see where it leads us.

The operator T_μ is said to be the **attenuated Radon (or X-ray) transform** (with attenuation $\mu(x)$) of the function $f(x)$.

The **attenuated backprojection** operator with attenuation $\nu(x, \omega) > 0$ (which may or may not be related to $\mu(x)$) acting on data $g(\omega, s)$ is

$$(T_\nu^\# g)(x) = \int_{|\omega|=1} g(\omega, x \cdot \omega) \nu(x, \omega) d\omega \quad (2)$$

In particular, if $\nu = 1$ (which we will assume in our experiments), this is the standard backprojection operator [19, 26, 27].

Let H be the Hilbert transform acting in variable s on functions $g(\omega, s)$:

$$Hg(\omega, s) = \frac{1}{\pi} v.p. \int \frac{g(\omega, r)}{s - r} dr.$$

Here $v.p.$ indicates that the integral is considered in the principal value meaning.

The following result holds:

Theorem 1. (see details in [21]) Let $f(x)$ be a function (our distribution of radiating sources) and μ be sufficiently smooth¹, then the operator

$$T_\nu^\# H \frac{d}{ds} T_\mu \quad (3)$$

applied to f preserves all singularities of f and does not create new ones. In particular, if f has a jump across an interface, the location of this jump is preserved in the image $T_\nu^\# H \frac{d}{ds} T_\mu f$.

Notice that $T_\nu^\# H \frac{d}{ds} T_\mu f$ is **not** a reconstruction of f from its measured projections $T_\mu f$ (which would be impossible anyway with the low signal strength and the attenuation μ being unknown), but it gives a correct reconstruction of all singularities (e.g., interfaces) of f .

Since we assume that our source is very small geometrically, almost a point source, it is rather singular, and thus one might expect that any guess for the unknown attenuation (e.g., that there is none) should reconstruct the location of the source correctly.

The operator

$$T_1^\# H \frac{d}{ds} \quad (4)$$

is exactly what is applied to the data in our experiments described below. We thus will not worry about the presence of an unknown attenuation.

The operator (4) is often called a **filtered backprojection (FBP)**, where $H \frac{d}{ds}$ and $T_1^\#$ are the filtration and backprojection parts, correspondingly.

There is a way in tomography to emphasize singularities of the function to be reconstructed. This is what the so called **local tomography** does (e.g., [9, 21]). For instance, the singularities will look brighter if one replaces the filtration part $H \frac{d}{ds}$ in (4) with a stronger filter $\frac{d^2}{ds^2}$:

$$T_1^\# \frac{d^2}{ds^2}. \quad (5)$$

This option will also be explored.

In the detection problem we are discussing, different types of particles (e.g., γ -photons of different energies) will be present, and each of them could have different distribution f_j of sources, as well as different attenuation distribution μ_j in the cargo. Thus, what we get if we lump all these particle counts together (which seems to be a strange thing to do), is the sum

$$g = \sum_j T_{\mu_j} f_j.$$

Can this complicate things? We claim that it should not. Indeed, all these functions have the same boundary of the source as their interface. Thus, one can derive from the above theorem the following

¹The detection procedures we eventually will come to will not request smoothness of attenuation.

Corollary 2. *Applying the same reconstruction operator $T_\nu^\# H \frac{d}{ds}$ to the whole sum, one still recovers the correct source interface, and, in fact, data from the different types of particles reinforce this reconstruction.*

It is still not clear whether such a procedure will work in our problem, since there are at least two potentially serious obstacles:

- The X-ray transform model does not apply when significant statistical noise is present, in particular for a very weak source.
- This model does not take into account presence of a very large (from standard tomographic point of view, enormous) background noise.

Still, we will try to apply this approach and see where it can lead us. We show below some sample results of numerical experimentation with the 2D and 3D X-ray transforms, as well as 3D Radon transform.

2.1 2D X-ray reconstructions

Although the problem is three-dimensional, for the first trial we consider the 2D problem, which is more straightforward to handle numerically.

In the first reconstruction we have modeled random γ -photon emission from a shielded ball of radius 4cm of *HEU235* for realistic values of the emission and attenuation rates. The ball was placed inside a much (about 100 times) larger “cargo” (the results for non-central locations of the source are similar). A uniform and isotropic random background was also added. The model included 64 detectors, each of which could detect 64 directional sectors (about 2.8 degrees each). In this reconstruction we assumed the SNR to be 1%, i.e. 99% of detected hits were generated by background, or scattered source particles. Then, the described above tomographic X-ray transform inversion (see (3) with $\nu = 1$) was applied to the resulting matrix of counts. The pictures below show the results of the reconstructions in 44×44 pixels (both the grey scale density and surface plots are presented). The result, shown in Fig. 2, shows clear detection of the source. We then try to lower the SNR towards our benchmark

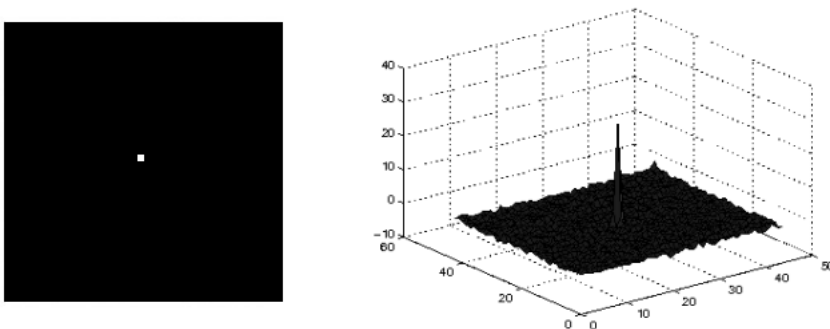


Figure 2: Reconstruction with SNR 1% (density and surface plots).

value 0.1%, and the success seems to evaporate. E.g., Fig. 3 shows the failed attempt of reconstruction with the SNR being 0.4% and with only about a hundred ballistic particles detected from the source.

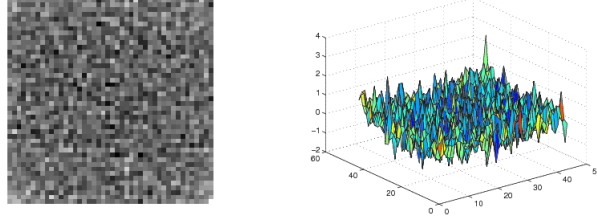


Figure 3: Unsuccessful FBP reconstruction with SNR 0.4% and about 100 ballistic source particles detected (density and surface plots).

In the previous examples we assumed that detectors were placed around the whole object of interest, which is not a very practical assumption. In the next example, the particles were detected by direction sensitive detector arrays placed along only three sides of a square containing the imaged object. This configuration resembles a “gate“, through which vehicles and cargo would pass. Each of the three detector arrays contained 100 detectors. The angular variable, which determines the direction of incident particles, was discretized into 200 angular bins. The number of detected source particles was 1039, versus 10^6 randomly distributed background particles. The source was located at $(0.203, -0.101)$. The results of the FBP (filtered backprojection) X-ray reconstruction are shown in Fig. 4. In this example, the SNR was of the order of

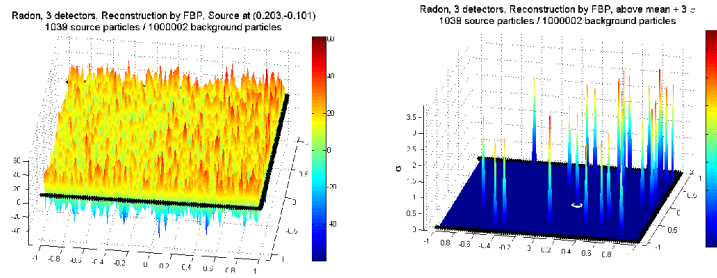


Figure 4: Filtered backprojection reconstruction from X-ray data measured by three detectors (left). The right picture shows only the peaks that are at least 3 standard deviations above the mean. The correct source location is encircled. SNR 0.1%.

our benchmark value 10^{-3} . One can see that, unfortunately, the reconstruction peaks not only at the correct source location but also at a number of other places. Even worse, some of those incorrect peaks are higher than the peak at the source. This is not that surprising, since we could not find the source even with higher SNR and surrounded with detectors in the previous example, and now we have smaller SNR and one detector missing. Can this situation be rectified?

Let us first try increasing the bulk number of detected particles. In the next example, we increased the total number of detected particles by 50% (which should increase chances of detection, as it is discussed in Section 3). Fig.5 shows the successful result of applying the filtered backprojection reconstruction of a source with the same SNR – 10^{-3} .

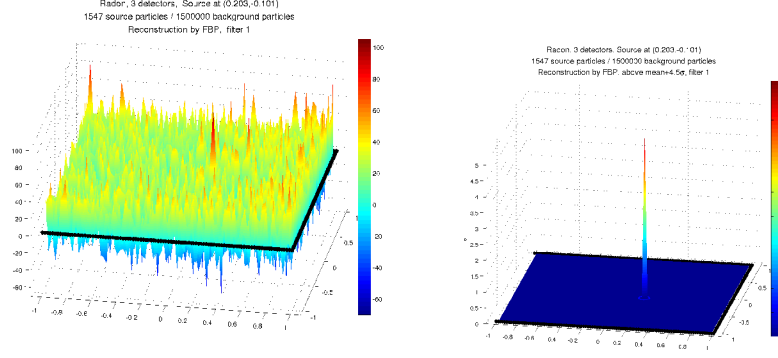


Figure 5: Filtered backprojection reconstruction from X-ray data measured by three detectors (left). The right picture shows only the peaks that are at least 4.5 standard deviations above the mean. The correct source location is encircled. SNR 0.1%, 1, 500, 000 background particles, 1547 source particles.

As we have already mentioned, the **local tomography** (which uses a stronger filter) emphasizes the singularities of an image, and thus one could expect it to detect our geometrically small sources better. This, however, is not the case, as, for instance, the next example (Fig. 6) shows. We use the same data as in the previous, successful FBP reconstruction.

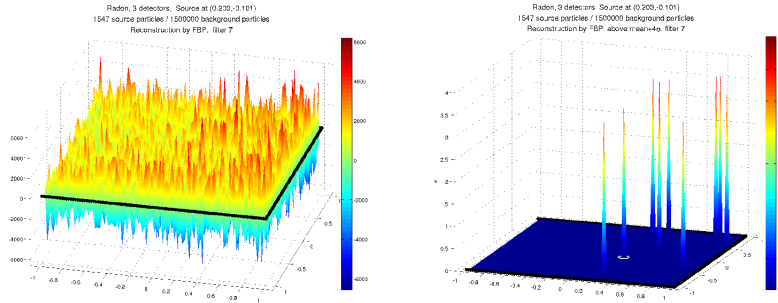


Figure 6: An example of local reconstruction with SNR .01%. The left picture shows the reconstruction. The right one shows only the values exceeding 3.5 standard deviations from the mean.

One can see that detection fails here. A stronger high-pass filter apparently just increased the contribution from the noise, so the image in fact worsened. This suggests that maybe one should try to eliminate the filtration step altogether and rely upon the backprojection alone.

We see in these examples that in 2D the FBP X-ray reconstructions of small low emission sources work somewhat, but appear to start failing before reaching our benchmark SNR when the total number of detected particles is about 10^6 . Local tomography makes things worse. However, just a backprojection and/or increasing the total number of detected particles bring some hope. This hope will be justified in Section 4

2.2 3D X-ray and Radon reconstructions

While in $2D$ there is a single transform that can be called interchangeably Radon transform or X-ray transform, these notions part in higher dimensions. In $3D$, there is the **X-ray transform**, which **integrates a function $f(x)$ over all straight lines** in \mathbb{R}^3 , as well as the **Radon transform**, which **integrates functions over all $2D$ planes**. Both are of interest in tomography, the first arising in X-ray CT scanners and the second in MRI imaging. In the situation we consider in this text, X-ray transform represents, the same way as it does in $2D$, the case of collimated detectors, while the Radon transform will have some relation to the Compton camera case considered in Section 5.

2.2.1 3D X-ray reconstructions

The same issues that we have discussed in $2D$ case remain: the X-ray transform model is valid only for strong sources (or long observation time) and it does not address the background noise. However, in $3D$ there is another feature that one has to take into account. Namely, while in $2D$ the set of lines is also 2-dimensional (the lines can be parametrized by their two normal coordinates), in $3D$ the space of lines is 4-dimensional. Thus, the X-ray data in $3D$ is redundant. In tomography, this redundancy is usually dealt with by selecting a 3-dimensional sub-set of data (the rest is not even collected). For instance, one can use only rays parallel to a fixed plane and do the reconstruction slice-by-slice, or one can pick only lines intersecting a given curve (often a helix). In the detection situation we are facing, this is not an option, since any attempt to reduce dimension of the data will essentially remove all signal and leave only noise in its wake. Thus, we need to use all, overdetermined data. This requires corresponding analytic formulas (which are easy to obtain and thus will not be introduced) and much heavier calculations.

Without further ado, we present an example (Fig. 7) of the FBP reconstruction, where 10^3 ballistic particles from the source and 1.35×10^6 background ones were detected.

Further experimenting with examples leads to the same conclusion as in $2D$: back-projection is superior to FBP in this situation, while local reconstruction leads to deterioration.

2.2.2 3D Radon reconstructions

In this section, we present some Radon transform reconstructions in $3D$. The reader should recall that the $3D$ Radon transform integrates functions over affine $2D$ planes, rather than lines. This is a preliminary test of the principle before doing $3D$ reconstructions for Compton cameras, where surface integrals (over cones) are also involved.

In the figures Fig. 8 – Fig 10 below, there were 10^6 background particles detected, while the number of ballistic particles from the source was varying, thus changing the SNR and the level of detectability. Density and surface plots of $2D$ sections through the source locations are shown. One sees that with the SNR of 0.5% the source can be detected, while at 0.1% and lower the detection deteriorates.

Let us see now whether backprojection alone does a better job. Figures 11 and 12 show the backprojection reconstruction from the same data as in Fig. 9 and 10. One

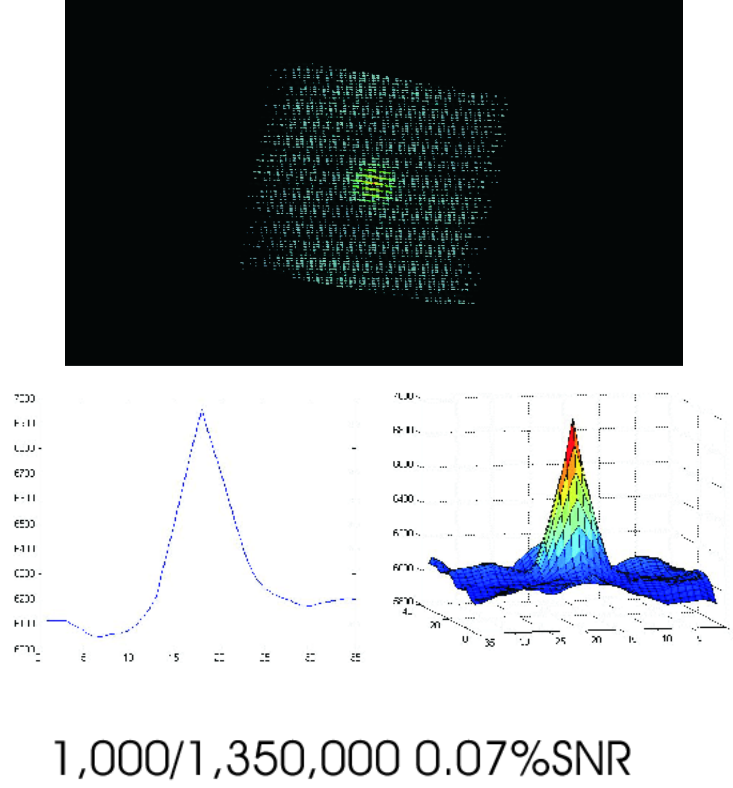


Figure 7: Here one sees a “transparent” 3D visualization, as well as pieces of 1D and 2D sections passing through the source.

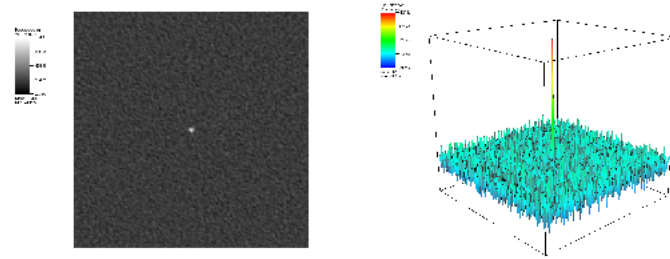


Figure 8: FBP reconstruction from 3D Radon data. 5000 ballistic source particles. SNR 0.5%.

clearly sees that the backprojection alone detects the source when the FBP method fails to do so.

Again, the examples above confirm the general feasibility of the approach and superiority of the backprojection.

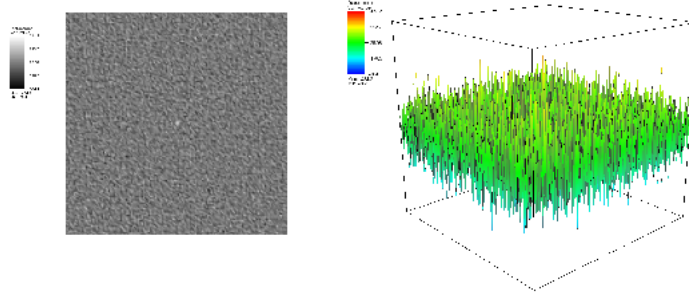


Figure 9: FBP reconstruction from 3D Radon data. 1000 ballistic source particles. SNR 0.1%.

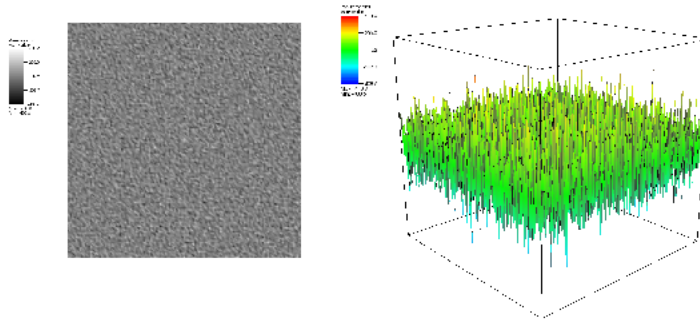


Figure 10: FBP reconstruction from 3D Radon data. 700 ballistic source particles. SNR 0.07%.

2.3 Discussion of the tomographic reconstructions

The experiments described in the previous sections beg several questions:

1. Why do tomographic methods still work to some degree, although the assumptions that lead to the X-ray transform model are not satisfied (i.e., the source is too weak) and a strong random background is present? Indeed, the use of standard tomography assumes that the data represents line integrals of the source distribution function. This is the same as to say that we measure the expectation of the number of hits, per unit time, from particles moving along a line. This assumption is reasonable when a substantial number of source particles is detected, i.e. when the source is strong, or the observation time is long. However, it fails in the case of low emission sources that cannot be observed for a really long time. Hence, the X-ray/Radon transform type models and techniques appear to be inappropriate.
2. Why does strengthening the filter (i.e., local tomography), which should increase detectability of singularities, makes the reconstruction worse?
3. Why do tomographic techniques fail to reliably detect sources at the levels of SNR and total number of particles for which the probabilistic consideration of

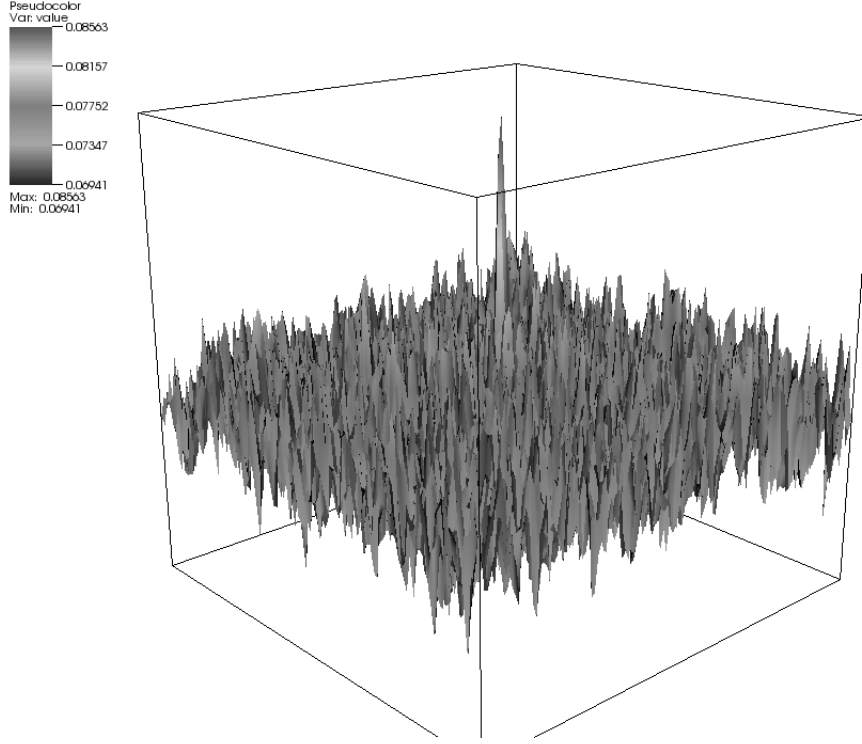


Figure 11: BP reconstruction from 3D Radon data. 1000 ballistic source particles. SNR 0.1%.

the next section suggests that sources should be detectable?

As we might have guessed already, the answer to the first question is that in fact, tomographic inversions do not work. Or, to put it differently, only a part of the algorithm (backprojection) works, while its other part (filtration) only hurts.

The answer to the second question is not hard to guess. Indeed, high-pass filters required in X-ray/Radon transform inversions amplify noise. This is a very significant factor, as the noise constitutes 99.9% of our data. Using local tomography can only aggravate this difficulty, and we have seen that it indeed does.

The answer to the third question is probably the same as the previous one: high-pass filters might be the culprits.

These considerations suggest to try to eliminate high-pass filtering completely, and thus to use backprojection alone (not a good idea in the standard imaging). We will see in the next sections that this is indeed the solution. Simultaneously, we will eliminate another drawback of the standard tomographic techniques, which is the difficulty of quantifying the confidence level of detection.

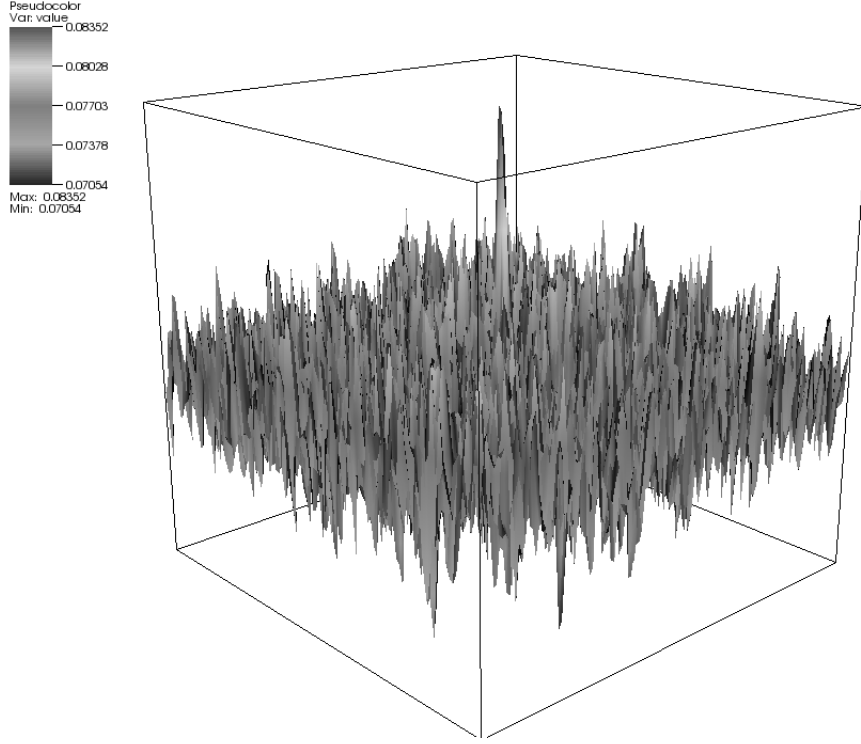


Figure 12: BP reconstruction from 3D Radon data. 700 ballistic source particles. SNR 0.07%.

3 A probabilistic discussion

Now we investigate why it *might* be possible to detect *geometrically small* low emission sources by backprojection. Let us suppose that the detectors are collimated and thus can determine information about the incident direction of particles. Then backprojection essentially “sends” the detected particles back along their incoming straight lines. In particular, these backpropagated trajectories of all ballistic source particles will pass through the source region. The background particles or the source particles that have scattered before reaching the detector, will be backprojected along straight lines, which are different from their original zig-zag trajectories, about which we have no knowledge. Therefore, in the considerations that follow, we assume that the backpropagated trajectories of these particles are random straight lines. We also assume for now that the random distribution of trajectories is uniform.

In a nutshell, our simple argument, which will be made more precise below, is that *if the number of lines passing through a tiny region exceeds significantly the mean of the background, then most probably there is a source at this location* (see Fig. 13).

Let us try to quantify this and consider N random particle trajectories in a ball B_R of radius R . What is the probability of at least n particles out of the total N contained in B_R to pass through a small ball B_r with radius r ? Let, as before, $L_{(\omega,s)}$ denote the line in \mathbb{R}^2 defined by its normal vector $\omega \in S^1$ and a signed distance s from the origin,

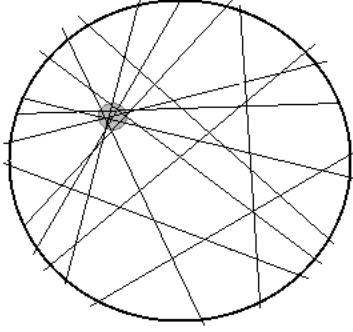


Figure 13: If the local density of lines is significantly higher in the gray region, this is likely due to a source being present at this location.

i.e.

$$L_{(\omega,s)} = \{\mathbf{x} \in \mathbb{R}^2 | \mathbf{x} \cdot \boldsymbol{\omega} = s, s \in \mathbb{R}, \boldsymbol{\omega} \in S^1\}.$$

Thus, the lines on the plane are mapped 1-to-1 to the points on the half-cylinder $S_+^1 \times (-\infty, \infty)$, where $S_+^1 = \{\boldsymbol{\omega} = (\cos \theta, \sin \theta), \theta \in [0, \pi)\}$, and these points are uniformly distributed on the half-cylinder. All lines intersecting B_R correspond to points on $S_+^1 \times (-R, R)$, and those intersecting B_r are bijectively mapped to points on $S_+^1 \times (-r, r)$. Thus, the probability of a random line in B_R passing through B_r is

$$p = \frac{\text{area}(S_+^1 \times (-r, r))}{\text{area}(S_+^1 \times (-R, R))} = \frac{r}{R}.$$

The probability that n out of the total N lines cross B_r is given by the Binomial distribution $B(N, p)$, and is equal to $\binom{N}{n} p^n (1-p)^{N-n}$. Since we are in the situation when p is fixed by the dimension of the source and N is large, the Central Limit Theorem applies. It follows that the Binomial distribution is approximated well by the Normal distribution $N(\mu, \sigma^2)$ with the mean $\mu = Np$ and standard deviation $\sigma = \sqrt{Np(1-p)}$. If it happens that the number of lines n crossing B_r exceeds significantly (in comparison with σ) the mean μ , the probability of this occurring just due to random reasons is very small. Therefore, one can be almost certain that this clustering of trajectories is the result of a radioactive source located at B_r . Our numerical experiments of source detection by backprojection agree with our expectations.

As an example, in Fig. 14 we present a typical histogram of the number of lines crossing a fixed pixel in the $2D$ unit square with a uniform grid of 100^2 pixels. Namely, the particles were detected by four arrays of collimated detectors placed on the sides of the square. The detected particles were backprojected, and the histogram of the backprojected pixel values was plotted. The signal to noise ratio was 0.001 and the number of background particles was 10^6 . On the far right of the histogram one sees the outlier contribution from the source, which deviates about 8.75 standard deviations from the mean. This result complies with discussion above: the presence of such a highly unlikely outlier indicates presence of a source.

Now we will make these statements more precise. Suppose that the area we are imaging is divided into N_{pix} pixels. Suppose further that n lines intersect a pixel B_r

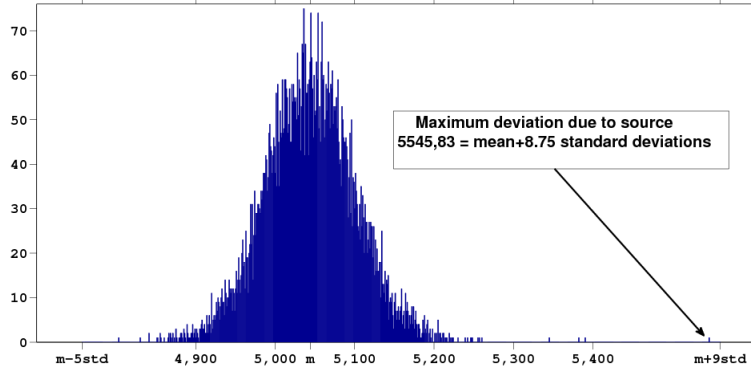


Figure 14: Histogram of a backprojection reconstruction from data collected by four collimated detectors, placed on the sides of the unit square. The data simulated a source at the point $(0.3, -0.4)$, with SNR 0.1% and total number of particles 1,001,000. The mean of the backprojected image is 5043.98, and the standard deviation is 57.37. The number of lines at the location of the source deviates 8.75 standard deviations from the mean.

with radius r . We will write $n = n_s + n_b$, where n_s and n_b are the number of ballistic source and background trajectories, respectively, which cross B_r . We will describe a method to determine whether there is a source located at this pixel.

Let us choose a threshold value k_t , such that the probability of a normal variable to reach more than k_t standard deviations above the mean is very small. E.g., $k_t = 5$ or higher suffices. If an abnormally high number n of lines passing through a pixel B_r is detected, i.e. if $n > n_t := \mu + k_t\sigma$, we will claim that the pixel contains a source. Otherwise, such claim will not be made. The probability of at least n_t lines crossing B_r due to random reasons is approximately $r := 0.5 \operatorname{erfc}(k_t/\sqrt{2})$. We also have to take into account the total number N_{pix} of pixels and the possibility of such clustering of lines occurring inside at least one of them. The probability of at least n_t lines crossing at least one of the pixels due to random reasons (and thus causing a "false alarm") can be approximated by

$$\text{fp rate} = 1 - (1 - r)^{N_{pix}}. \quad (6)$$

Here *fp rate* stands for *false positive rate*, which is the rate of false detections [10]. We must note that the above estimate assumed independence for different pixels of the events "the pixel is crossed by n lines". This is, obviously, not the case, but more precise estimates would be more complicated and would not make a significant difference in what follows next (much cruder estimates exist and can be used).

The *true negative rate* (or specificity), is given by

$$\text{tn rate} = 1 - \text{fp rate}$$

and represents the rate of correctly classified negative outcomes. The true negative rate is also the confidence probability that we have found a true source. We will write

$$\text{tn rate} = \text{confidence} := (1 - r)^{N_{pix}} = [1 - 0.5 \operatorname{erfc}(k_t/\sqrt{2})]^{N_{pix}}. \quad (7)$$

In particular, if the threshold value k_t is set to 5 and there are 100^2 pixels, the true negative rate is .997, which gives also this number as the confidence that the alleged

sources are indeed true. This confidence probability depends only on the pre-set threshold value k_t of the method and the number of pixels N_{pix} . However, if in some pixel the number of lines deviates from the mean even further, this increases the confidence probability that there is indeed a source there. For instance, if $n \geq \mu + 7\sigma$, the confidence reaches, for all practical purposes, 100%.

Let us discuss now the probability of missing a source. We assume that an *a priori* ballpark estimate of possible value of n_s (the number of ballistic particles coming from the source) is available. We can measure n_s in the σ units:

$$n_s = k_s \sigma.$$

Here k_s is a positive constant and σ is the standard deviation of the distribution of the number of background trajectories passing through a pixel². Now suppose that there is indeed a source present in a pixel B_r . How can we miss it? Since our test identifies a source whenever $n = n_s + n_b > \mu + k_t \sigma$, the necessary condition for missing it is

$$n < \mu - (k_s - k_t) \sigma.$$

The probability of this happening (i.e., the *false negative rate* (fn rate)) is given by

$$\text{fn rate} = 0.5 \operatorname{erfc} \left(\frac{k_s - k_t}{\sqrt{2}} \right). \quad (8)$$

For instance, if $k_s \geq k_t + 3$, the probability of missing this source is at most 0.0013.

The sensitivity, or *true positive rate* (tp rate), is given by

$$\text{tp rate} = 1 - \text{fn rate}.$$

Note that the sensitivity of the method depends on the threshold value k_t as well as on our estimate of detected source particles.

From the above discussion we see that in order to find sources reliably, it suffices to detect $n_s > (k_t + 3)\sigma$ ballistic particles from the source.

We claim that **for any given SNR $s > 0$ and for any $k_t > 0$ it is possible to detect the source, provided that the total number of detected particles, N , is sufficiently large.**

Indeed, if a signal to noise ratio s is known, and if $p \ll 1$, the number of detected source particles will be $n_s \approx sN$ and $\sigma \approx \sqrt{Np(1-p)}$. Then, we require the following inequality to be satisfied:

$$sN > (k_t + 3) \sqrt{Np(1-p)}. \quad (9)$$

Since the left hand side of (9) grows linearly with N and the right hand side grows only as \sqrt{N} , the inequality will be satisfied for a sufficiently large N . We come up with the following rule of thumb:

One can expect to detect reliably the source with high sensitivity and specificity, if the total particle count N at the detectors is on the order of

$$N \propto \left(\frac{8}{s} \right)^2 p(1-p), \quad (10)$$

² Recall that σ is determined by the total number of detected particles, which is known, and the ratios of the source dimension to the dimension of the imaged region, for which we would, in practice, have a crude idea.

or higher, where s is the SNR (ballistic particles from the source vs the total hits) and $p = r/R$, where r and R are the linear dimensions of the source and the whole area correspondingly.

Let us play with some practically possible values of the parameters. A nuclear source with shielding could have a radius of the order of several centimeters, while a vehicle or a cargo container has size in the order of meters. Thus, we will assume that

$$R = 1, r = 0.01 \Rightarrow p = 10^{-2}. \quad (11)$$

Substituting this value of p and $s \approx 10^{-3}$, one expects that when N reaches close to 10^6 and directional information at detectors is available, the sources should be reliably detectable. This squares well with the results of our previous computations with the backprojection methods (FBP falls somewhat short of this).

The conclusion from this probabilistic discussion is that the simple backprojection should reliably detect sources with low SNR, as long as the total number N of detected particles is high enough (see (10)). E.g., for the SNR of about 0.1% the values of N around 10^6 should be sufficient. Besides, the confidence probability of detection (or absence of a source) can be computed.

The use of backprojection should also smooth out unstructured noise. In the next section we present numeric examples of such backprojection detections.

It is worthwhile to notice that, as long as the threshold parameter k_t (equivalently, the desired confidence probability) is fixed, the whole detection procedure can be done automatically, without necessity of a human eye assessment of the reconstruction.

4 Source Detection Using Backprojection

We illustrate the conclusions of the previous Section on a typical example of 2D X-ray data. In fact, the data used for this backprojection reconstruction was the same that was used for the unsuccessful FBP reconstruction shown on Fig. 4. We assume three detector arrays located along three sides of a square. Such a “detector gate” is a more realistic configuration than detectors surrounding the whole object. The incoming trajectories of detected particles from each of the three detector arrays were backprojected separately and then the results were added. The first picture Fig. 15 shows a typical backprojection reconstruction. The drop of the values at one side of the square is due to detectors missing there. Thus, effectively, there is a non-uniform distribution of the background, which contradicts to our assumption of uniformity. However, this non-uniformity is smooth, so we can assume that *locally* the distribution of background trajectories is uniform. In order to apply our probabilistic arguments described in Section 3 we estimate the *local* mean and standard deviation at every point. For the reconstruction shown on Fig.15, this was done by analyzing the data on a 7×7 sub-grid surrounding each pixel. Then, the local means were subtracted and the resulting values plotted (see the bottom left picture in Fig. 15) in the units that are equal to the standard deviation σ (see the discussion in the previous section). Finally, the values below the threshold $k_t = 3.5$ were erased (bottom right in Fig. 15). The result clearly shows the detected source. The confidence probability was calculated as

$$\text{confidence} = (1 - 0.5 * \text{erfc}(k_{\text{source}}/\sqrt{2}))^{100^2},$$

where k_{source} is the height of the highest peak. The calculated confidence level for this example was 99.99%. Notice that if we used the threshold value $k_t = 3.5$ instead of the actual peak's height, we would have significantly underestimated the confidence.

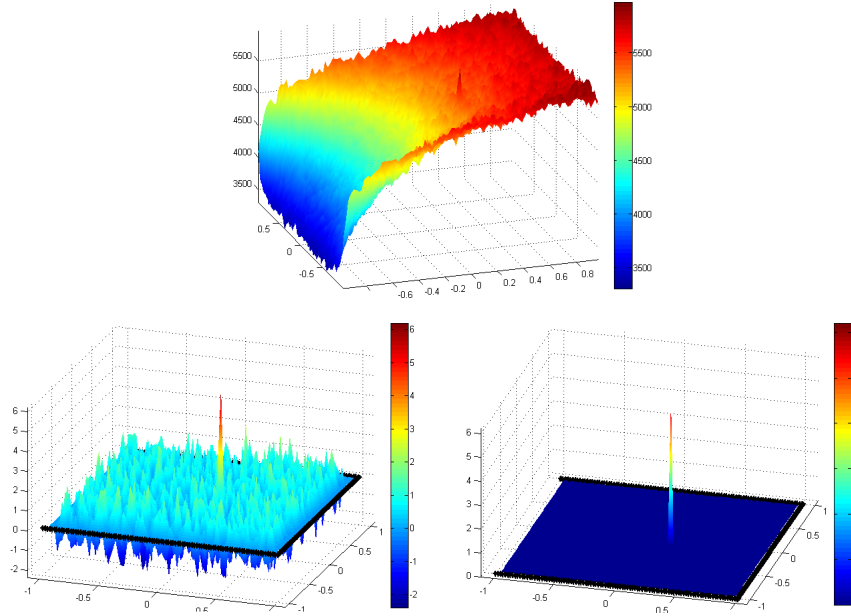


Figure 15: Backprojection reconstruction from X-ray data (top). The unit on the vertical axis in the bottom pictures is one (local) standard deviation from the (local) mean. Bottom left picture shows the result of backprojection after subtraction of the local mean. Peaks that exceed the local mean by more than 3.5 (local) standard deviations are shown at bottom right. Source located at (0.203, 0.101) is detected with confidence 99.99%.

5 Compton Cameras

Compton cameras, also called Compton scatter cameras or electronically collimated cameras, have received a lot of attention since they were first proposed in [40] and a prototype was developed in [35, 36]. Compton cameras were first suggested for use in nuclear medicine (SPECT), but they also have applications in astrophysics [13, 37, 43], monitoring nuclear power plants [32, 33], and other areas. Compton cameras offer several advantages over the conventional mechanically collimated (Anger) γ -cameras. The most significant of these is the dramatic increase of sensitivity – Compton cameras are reported to count orders of magnitude more photons than Anger cameras [5, 23]. Another advantage is the flexibility of geometrical design [32, 33], which even allows for hand-held devices [16, 22].

A Compton camera consists of two detectors, which, in the standard setup, are planar and are placed one behind the other (see Fig. 16). A photon incident on the camera undergoes Compton scattering in the first detector, which records the location x_1 and the energy of interaction E_1 . After the scattering, the photon is absorbed in

the second detector, where the position x_2 and energy of absorption E_2 are measured. From the knowledge of E_1 and E_2 , the scattering angle ψ can be determined by the

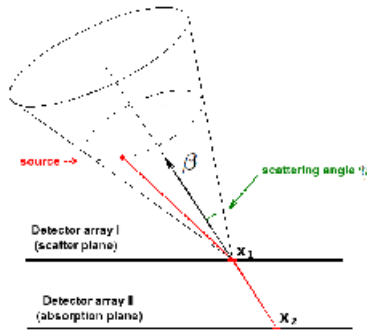


Figure 16: Schematic representation of a Compton camera.

formula (e.g. [6, 40])

$$\cos \psi = 1 - \frac{mc^2 E_1}{(E_1 + E_2)E_2}. \quad (12)$$

Here m is the mass of an electron and c is the speed of light. The direction into which a photon scatters is given by $-\beta := \frac{\mathbf{x}_2 - \mathbf{x}_1}{|\mathbf{x}_2 - \mathbf{x}_1|}$. From the knowledge of β and the scattering angle ψ we conclude that the photon originated from the surface of the cone with central axis β , vertex \mathbf{x}_1 and opening angle 2ψ . Therefore, although the exact incoming direction of the detected particle is not available, one knows a cone of such possible directions. The goal of Compton camera imaging is to recover the distribution of the radiation sources from this data.

The description above addresses the Compton γ -cameras only. However, neutron detectors are currently being developed [24, 39] that (employing a different physics principle) provide the similar cone information. We thus will not make distinction between these and call them all “Compton type cameras.”

We will now address briefly the mathematics behind the Compton type measurements.

5.1 The Cone Transform

Suppose that we want to image the distribution $f(\mathbf{y})$ of radioactivity sources inside a certain object in \mathbb{R}^3 . From now on, we will assume that $f(\mathbf{y})$ is supported on one side of the Compton camera and that $\text{supp} f$ does not intersect the camera. Under the assumption of a sufficiently long observation time (and thus a large number of photons detected), the Compton camera provides us with the projections [1, 6, 42], which we denote by $\mathcal{C}f(\mathbf{x}, \beta, \psi)$, i.e. the integrals of $f(\mathbf{y})$ over cones parameterized by a vertex \mathbf{x} lying on the detector, central axis vector β from the unit sphere S^2 , and half-angle $\psi \in [0, \pi]$ (see Fig.17):

$$\mathcal{C}f(\mathbf{x}, \beta, \psi) = K(\psi) \int_0^{2\pi} \int_0^\infty f(\mathbf{x} + r\alpha(\phi)) r \sin \psi \, dr \, d\phi, \quad \alpha \cdot \beta = \cos \psi, \quad \alpha \in S^2. \quad (13)$$

Here $K(\psi)$ is the Klein-Nishina distribution of scattering angles³. The function $\mathcal{C}f(\mathbf{x}, \boldsymbol{\beta}, \psi)$ provides the expectation of the number of hits, per unit time, from the particles moving along the cone. In particular, when the particle count is low, these values are not well determined by the data. This issue was addressed in the preceding Sections. An im-

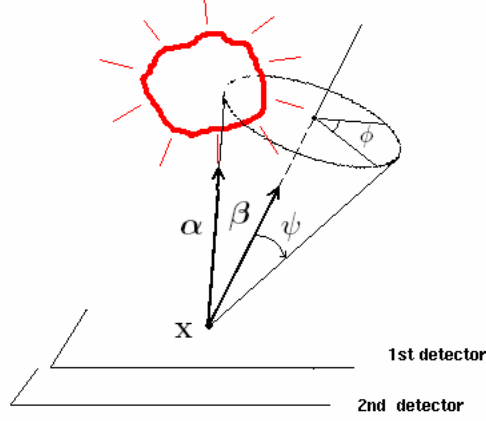


Figure 17: A Compton cone with apex \mathbf{x} , central axis $\boldsymbol{\beta}$ and half-angle ψ .

portant observation is that the problem of inverting the cone transform $\mathcal{C}f(\mathbf{x}, \boldsymbol{\beta}, \psi)$ is even more overdetermined than the 3D X-ray transform. Indeed, $f(\mathbf{y})$ is a function of three variables, while $\mathcal{C}f(\mathbf{x}, \boldsymbol{\beta}, \psi)$ depends on five parameters (here \mathbf{x} is restricted to a 2D detector surface). Most authors consider restricted versions of the cone transform, reducing the number of parameters from five to three [1, 6, 28]. The paper [38] contains a closed form inversion formula, which uses four of the parameters⁴. We, however, have to use the full 5-dimensional dataset, since, as it was mentioned before, any attempt to restrict the data would wipe out the signal.

5.2 Reconstruction Techniques in Compton Camera Imaging

We provide here a brief survey of some known reconstruction methods in Compton cameras imaging. Many of them reduce cone projections to Radon projections, i.e. integrals of f over planes.

Algebraic Reconstruction Techniques, as elsewhere in tomography, are widely used in Compton cameras imaging. This is partially due to the fact that analytic inversion formulas were not available until the second half of 1990's. Maximum likelihood methods were developed in [3, 7, 14]. A maximum likelihood method was also used in imaging with the COMPTEL telescope [37]. In [34] a matrix inversion technique was utilized to solve the problem for a specific detector geometry. Fast backprojection algorithms were developed in [31, 44].

³The Klein-Nishina factor is a known function and thus can be easily accounted for. We therefore do not include it in the further analysis.

⁴Recently [25], the complete set of data was used for reconstructions.

A *spherical harmonics expansion* solution was proposed in [1]. For every point \mathbf{x} on the detector array, and a fixed in advance half-angle ψ the authors relate the conical projection $\mathcal{C}f(\mathbf{x}, \boldsymbol{\beta}, \psi)$ to the Radon projection (integral) of f over the plane passing through x and perpendicular to $\boldsymbol{\beta}$. A fast algorithm for computing the spherical harmonic series was also developed in this paper. Several other authors provided spherical harmonics solutions, however their model for Compton data differs from (13), e.g. [18, 30, 41].

Probably the first *closed form analytic inversion formula* was obtained in [6]. The authors considered only cones perpendicular to the detector plane, i.e. cones with central axis $\boldsymbol{\beta} = \mathbf{z}$. Thus, the Compton data depends only on the vertex $\mathbf{x} := (x, y)$ and the opening angle ψ . Let us denote $g(x, y, \psi) := \mathcal{C}f(\mathbf{x}, \mathbf{z}, \psi)$ and let $F(u, v, \cdot)$, $G(u, v, \cdot)$ be the two-dimensional (x, y) -Fourier transforms of $f(x, y, z)$ and $g(x, y, \psi)$ respectively. Then the following relation holds:

$$F(u, v, \frac{\xi}{\sqrt{u^2 + v^2}}) = \mathcal{H}_0 \left[\frac{u^2 + v^2}{K(t)t\sqrt{1+t^2}} G(u, v, t) \right] \Big|_{t=\xi}, \quad (14)$$

where $\xi = z\sqrt{u^2 + v^2}$ and $t = \tan \psi$. Here \mathcal{H}_0 is the zero-order Hankel transform

$$\mathcal{H}_0 g(\rho) = 2\pi \int_0^\infty g(r) r J_0(2\pi r \rho) dr,$$

and $J_0(\gamma) = (2\pi)^{-1} \int_0^{2\pi} e^{i\gamma \cos \phi} d\phi$ is the zero-order Bessel function. Later, in [29], more properties of the same restricted cone transform were given.

In [25] the authors use yet another mathematical formulation for the forward problem, which accounts for the efficiency of the detector at different incident angles of particles. They extended the approach of [6] to show that the radioactivity distribution can be reconstructed from any family of cones that have central axes $\boldsymbol{\beta}$ such that the angle between $\boldsymbol{\beta}$ and the \mathbf{z} -axis is fixed. Then averaging of the solutions for different values of this angle was employed, thus making use of all available data and reducing noise.

The following useful relation between the cone and Radon transforms was found in [38]:

$$HRf(\boldsymbol{\beta}, \mathbf{x} \cdot \boldsymbol{\beta}) := \frac{1}{\pi} \int_{-\infty}^{\infty} Rf(\boldsymbol{\beta}, t) h(\mathbf{x} \cdot \boldsymbol{\beta} - t) dt = -\frac{1}{\pi} \int_0^\pi \mathcal{C}f(\mathbf{x}, \boldsymbol{\beta}, \psi) h(\cos \psi) d\psi \quad (15)$$

Here H denotes the Hilbert transform and R is the Radon transform in three dimensions. Note that four out of five variables are used and that the $HRf(\boldsymbol{\beta}, \mathbf{x} \cdot \boldsymbol{\beta})$ is constant on the line $L_c := \{\mathbf{x} \in \text{detector plane} | \mathbf{x} \cdot \boldsymbol{\beta} = c\}$, for any fixed constant c . The last observation shows that it is possible to reconstruct f if the vertices of cones \mathbf{x} are restricted to a curve. This also allows for averaging of the solution on the lines L_c . In Section 6.1 we will consider a two-dimensional analog of this formula.

6 Compton Cameras in Two Dimensions

In the two dimensional setting we assume that the detectors \mathbf{x} lie on a line, which we call the *detector line*. A cone in two dimensions is defined by a point \mathbf{x} that serves as

its vertex, a central axis unit vector β , and a half-angle ψ . Such cones simply consist of two rays with a common vertex. More precisely, let $\beta = (\cos \beta, \sin \beta) \in S^1$, $\beta \in [0, \pi]$ be the central axis of a cone with opening half-angle $\psi \in [0, \pi]$. The two half-lines that constitute the cone pass through the detector point \mathbf{x} and are given by

$$\{\mathbf{y} \in \mathbb{R}^2 : \mathbf{y} = r\alpha_i, r \geq 0\}, i = 1, 2,$$

where $\alpha_1 = (\cos(\beta - \psi), \sin(\beta - \psi))$ and $\alpha_2 = (\cos(\beta + \psi), \sin(\beta + \psi))$, see Fig. 18. As we have agreed before, we drop the known factor $K(\psi)$. Thus, in what follows we will assume uniform distribution of scattering angles, that is $K(\psi) \equiv 1$. Then the two dimensional cone transform $\mathcal{C}f(\mathbf{x}, \beta, \psi)$ is the projection of $f(\mathbf{y})$ onto these lines:

$$\mathcal{C}f(\mathbf{x}, \beta, \psi) = \int_0^\infty (f(\mathbf{x} + r\alpha_1) + f(\mathbf{x} + r\alpha_2)) dr = \mathcal{D}f(\mathbf{x}, \alpha_1) + \mathcal{D}f(\mathbf{x}, \alpha_2). \quad (16)$$

Here $\mathcal{D}f(\mathbf{x}, \alpha) = \int_0^\infty f(\mathbf{x} + r\alpha) dr$ denotes the divergent beam (or fanbeam) transform of f .

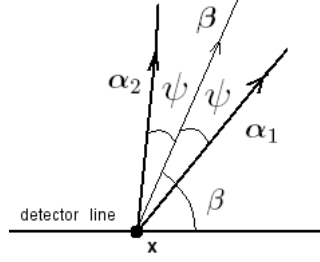


Figure 18: Two-dimensional cone with apex \mathbf{x} , central axis β and half-angle ψ .

For convenience, we will sometimes express $\mathcal{C}f$ and $\mathcal{D}f$ as functions of the angle β instead of the unit vector β . Thus, we can write (16) as

$$\mathcal{C}f(\mathbf{x}, \beta, \psi) = \mathcal{D}f(x, \beta - \psi) + \mathcal{D}f(x, \beta + \psi). \quad (17)$$

As in 3D, the problem of inverting the two-dimensional transform is overdetermined: $\mathcal{C}f(\mathbf{x}, \beta, \psi)$ depends on three parameters, while $f(\mathbf{y})$ only on two.

The authors are aware of few papers devoted to Compton cameras in two dimensions. In [2, 12] subsets of the cone projections of $f(x)$ are represented as line integrals of the function f added with its mirrored shear transformation. Namely, let us introduce the variables $k_1 = \cot(\beta + \psi)$, $k_2 = \cot(\beta - \psi)$. The cone transform can be written as

$$\mathcal{C}f(x, \beta, \psi) = \int_0^\infty f(x + k_1 z, z) dz + \int_0^\infty f(x + k_2 z, z) dz, \quad (18)$$

where the x -axis coincides with the detector line and the z -axis is perpendicular to the detectors. Let us fix the sum $k_1 + k_2 = K$ and define the function

$$f_K(x, z) = \begin{cases} f(x, z), & \text{if } z \geq 0 \\ f(x - Kz, -z), & \text{if } z < 0. \end{cases} \quad (19)$$

Then, $\mathcal{C}f(x, \beta, \psi) = \int_{-\infty}^{\infty} f_K(x + k_1 z, z)$. Thus, for each fixed value of K , the cone projections are represented as line integrals of a certain function, so all that remains is to invert the Radon transform. The reconstructed image will contain the function f above the detector line and a mirrored shear transformation of f below the detectors. Obviously, by fixing the parameter K , not all available data is used. The case when $K = 0$ corresponds to using only those cones with central axes orthogonal to the detector line. Since we need to use all overdetermined data, this approach is inconvenient. Besides, as our previous consideration of tomographic methods shows, in our specific situation, backprojection methods, rather than attempting the “full” reconstruction should be used.

6.1 Three Inversion Methods

6.1.1 Method A

The following relation, proven in [17], makes use of all parameters and is an analog of the three dimensional result presented in [38].

Theorem 3. *Let the closed unit ball lie on one side of and away from the detector line, and let $f(x) \in H_0^{1/2}(B^2)$. Denote $h(t) = 1/t$. Then*

$$H\mathcal{R}f(\mathbf{x} \cdot \boldsymbol{\beta}, \boldsymbol{\beta}) = \frac{1}{\pi} \int_{-\infty}^{\infty} \mathcal{R}f(\boldsymbol{\beta}, t) h(\mathbf{x} \cdot \boldsymbol{\beta} - t) dt = -\frac{1}{\pi} \int_0^{\pi} \mathcal{C}f(\mathbf{x}, \boldsymbol{\beta}, \psi) h(\cos \psi) d\psi \quad (20)$$

Here H is the Hilbert transform in the first (scalar) variable and the integrals are understood in the principal value sense.

Here B^2 is the unit disk in the plane and H_0^s is the standard notation for Sobolev spaces (e.g., [8]).

Corollary 4. *Theorem 3 provides an inversion formula for the cone transform.*

Indeed, computing the integral in the right hand side of (20), one recovers $H\mathcal{R}f$, where \mathcal{R} is the 2D Radon transform, and H is the Hilbert transform with respect to the linear variable. Then, the filtered backprojection formula for inversion of the two-dimensional Radon transform,

$$f(x) = \frac{1}{4\pi} \mathcal{R}^{\#} \left(H \frac{\partial}{\partial s} \mathcal{R}f \right) (x), \quad (21)$$

implies that after differentiating the right hand side of (20) with respect to the linear variable and backprojecting, one recovers the function f .

Remark 5. *In the left hand side of (20), one sees $\mathcal{R}f(s, \boldsymbol{\beta})$, where $s = \mathbf{x} \cdot \boldsymbol{\beta}$. Thus, if one infinite detector array is used and $\boldsymbol{\beta}$ is perpendicular to the array, we would only know $\mathcal{R}f(s, \boldsymbol{\beta})$ for a single value of s . If the detector array is finite, as is the case in all implementations, we would miss a much bigger chunk of data. One possible way to obtain the complete Radon data in $(s, \boldsymbol{\beta}) \in [-1, 1] \times S^1$ is, for example, to use three finite size detector arrays placed along the sides of a square containing the object.*

6.1.2 Method B

Another, simpler way of obtaining Radon data from cone data is presented below. Let us denote by $u(\mathbf{x}, \alpha)$ the integral of f along the ray starting at the point \mathbf{x} in direction of the unit vector α (i.e. the fanbeam projection of f):

$$u(\mathbf{x}, \alpha) = \mathcal{D}f(\mathbf{x}, \alpha) := \int_0^\infty f(\mathbf{x} + r\alpha) dr. \quad (22)$$

Let us fix a detector position \mathbf{x} and a direction α_0 and try to recover the fanbeam data $u(\mathbf{x}, \alpha_0)$. For any $\psi \in [-\pi, \pi]$ we can write $\mathcal{C}f(\mathbf{x}, \beta, |\psi|) = u(\mathbf{x}, \beta - |\psi|) + u(\mathbf{x}, \beta + |\psi|)$. Thus, the following relation holds

$$u(\mathbf{x}, \alpha_0) = \mathcal{C}f(\mathbf{x}, \alpha_0 + \psi, |\psi|) - u(\mathbf{x}, \alpha_0 + 2\psi)$$

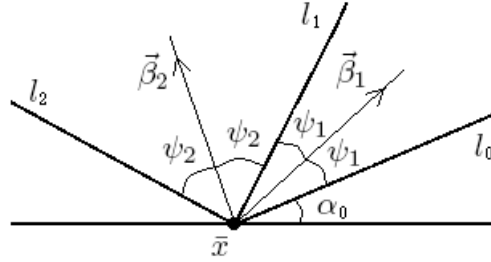


Figure 19: In order to determine the integral of f along the line l_0 , add the integral over the cone consisting of l_0 and l_1 to the integral over the cone determined by l_0 and l_2 . Then subtract the integral over the cone determined by l_1 and l_2 .

It is easily seen now (Fig. 19) that for any two half-angles $\psi_1, \psi_2 \in [-\pi, \pi]$ the fanbeam data $u(\mathbf{x}, \alpha_0)$ can be obtained from cone data as follows:

$$\begin{aligned} u(\mathbf{x}, \alpha_0) = & \\ & \frac{1}{2} [\mathcal{C}f(\mathbf{x}, \alpha_0 + \psi_1, |\psi_1|) + \\ & \mathcal{C}f(\mathbf{x}, \alpha_0 + \psi_2, |\psi_2|) - \mathcal{C}f(\mathbf{x}, \alpha_0 + \psi_1 + \psi_2, |\psi_1 - \psi_2|)] \end{aligned} \quad (23)$$

The angles ψ_1 and ψ_2 were arbitrarily chosen, so one could average on ψ_1 and ψ_2 in order to use all available data. This averaging also helps reducing the effects of the background noise.

If averaging over half-angles ψ_1 and ψ_2 is used, this method is computationally expensive. We propose a third reconstruction method, which is fast and makes use of all available data.

6.1.3 Method C

Let us recall that the source intensity function $f(\mathbf{y})$ is compactly supported and $\text{supp } f$ lies on one side and away from the detector array. Let us fix a detector location \mathbf{a} .

Then function $u(\mathbf{a}, \alpha)$ (see (22)) is supported in $(0, \pi)$. The function $u(\mathbf{a}, \alpha)$ can be extended periodically in α from $[0, 2\pi]$ to $(-\infty, \infty)$. Let us define

$$\tilde{u}(\mathbf{a}, \alpha) := \pi^{-1} \int_{-\alpha}^{\pi-\alpha} \mathcal{C}f(\mathbf{a}, \alpha + \psi, |\psi|) d\psi \quad (24)$$

We can write,

$$\begin{aligned} \tilde{u}(\mathbf{a}, \alpha) &= \pi^{-1} \left\{ \int_{-\alpha}^{\pi-\alpha} u(\mathbf{a}, \alpha) d\psi + \int_{-\alpha}^{\pi-\alpha} u(\mathbf{a}, \alpha + 2\psi) d\psi \right\} = \\ &= u(\mathbf{a}, \alpha) + (2\pi)^{-1} \int_0^{2\pi} u(\mathbf{a}, \alpha) d\alpha \end{aligned} \quad (25)$$

In the above equation, the periodicity of $u(\mathbf{a}, \alpha)$ with respect to α was used. Then,

$$\begin{aligned} \tilde{u}(\mathbf{a}, \alpha) &= u(\mathbf{a}, \alpha) + \frac{1}{4\pi} \int_{|\boldsymbol{\omega}|=1} \int_{-\infty}^{\infty} f(\mathbf{a} + r\boldsymbol{\omega}) dr d\boldsymbol{\omega} \\ &= \mathcal{D}f(\mathbf{a}, \alpha) + (4\pi)^{-1} (\mathcal{R}^\# \mathcal{R}f)(\mathbf{a}). \end{aligned} \quad (26)$$

Here, as before, $\mathcal{R}^\#$ denotes the backprojection operator

$$\mathcal{R}^\# g(\mathbf{y}) = \int_{|\boldsymbol{\omega}|=1} g(\mathbf{y} \cdot \boldsymbol{\omega}, \boldsymbol{\omega}) d\boldsymbol{\omega}.$$

The second term in the right-hand side of (26) can be written as

$$\mathcal{D}[(4\pi)^{-1} \mathcal{R}^\# \mathcal{R}f(\mathbf{a}) \delta(\mathbf{a} - \mathbf{y})],$$

where δ is the Dirac's delta-function. Therefore, we come to the following conclusion:

Theorem 6. *When the inverse fan-beam transform is applied to \tilde{u} , the result equals the sum of the function $f(\mathbf{y})$ and a distribution supported on the detector array only. Hence, functions f supported away from the detector arrays are recovered correctly.*

7 2D Compton data backprojection examples

For the reconstruction from Compton camera data presented in this section, we used Method C, described in Section 6.1.3, to convert the cone data into X-ray data. This method is chosen as the least computationally expensive and also using all cone data. After that, the reconstruction procedures were employed.

One expects that Compton data reconstructions will not do better than more precise (collimated) X-ray data. We will see, however, that the quality of these reconstructions is quite comparable.

In the next example we used filtered backprojection to reconstruct the source distribution. On Fig. 20 a reconstruction from data obtained by three Compton cameras is shown. The number of detected source particles was 1039, versus 10^6 background particles. The source was located at $(0.203, -0.101)$. The disappointing result is similar to the one we had in the X-ray case: many spurious sources are detected.

The backprojection, rather than FBP reconstruction, from the same data used in Fig. 20 is shown on Fig. 21. The results are similar to the reconstruction from X-ray data: the source is now convincingly detected. However, the confidence probability is

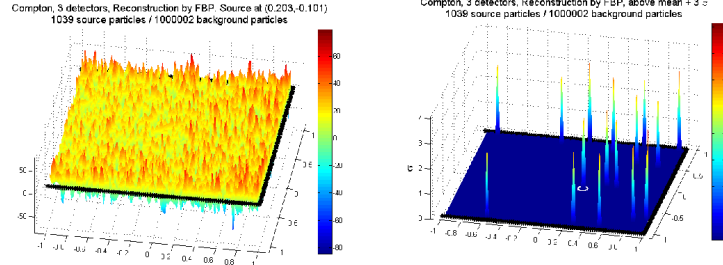


Figure 20: Filtered backprojection reconstruction from Compton data (left). The black lines represent the detectors. The right picture shows only the peaks that deviate more than 3 standard deviations from the mean. The correct source location is encircled.

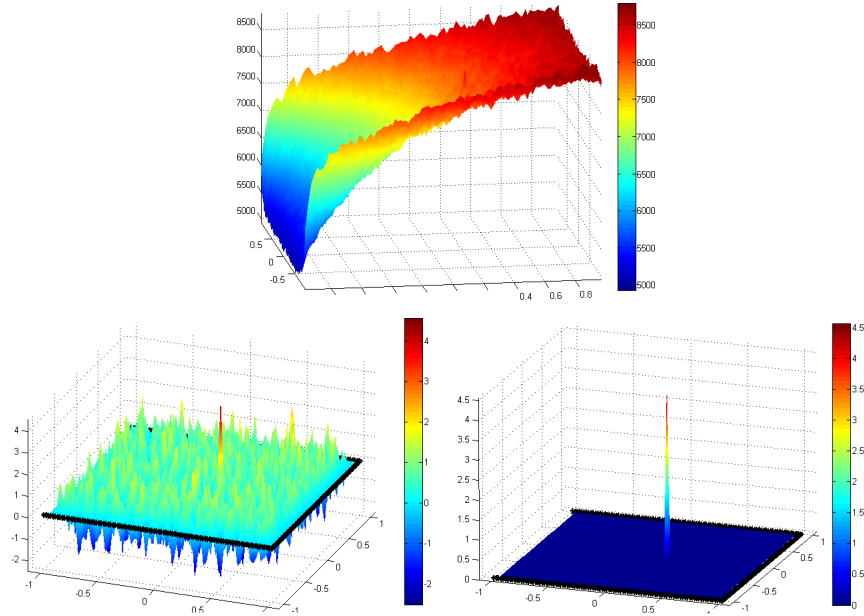


Figure 21: Unprocessed backprojection reconstruction from Compton data (top). The bottom left shows deviations from the (local) mean, measured in the units of (local) standard deviations. Only the peaks that exceed the mean more than 3.5 (local) standard deviations are shown on bottom right. Source located at (0.203, 0.101) is detected with confidence 97.56%.

slightly lower - 97.56%. This reflects the somewhat lower quality of Compton data in comparison with the data from collimated cameras.

A few more examples of reconstructions from Compton camera data are provided below.

For the next example, the number of source particles was 986 versus 10^6 background particles. The source in Fig. 22 is close to one detector array. The local mean and standard deviation were estimated on a larger local grid, 11×11 pixels, which raised the confidence level. We believe that larger local grids allow for more precise estimation

of the mean, thus raising the confidence level for the detected source. However, if the local grids are too large, the distribution of trajectories in a local grid would not be close to uniform anymore, and this will hamper our ability for detection.

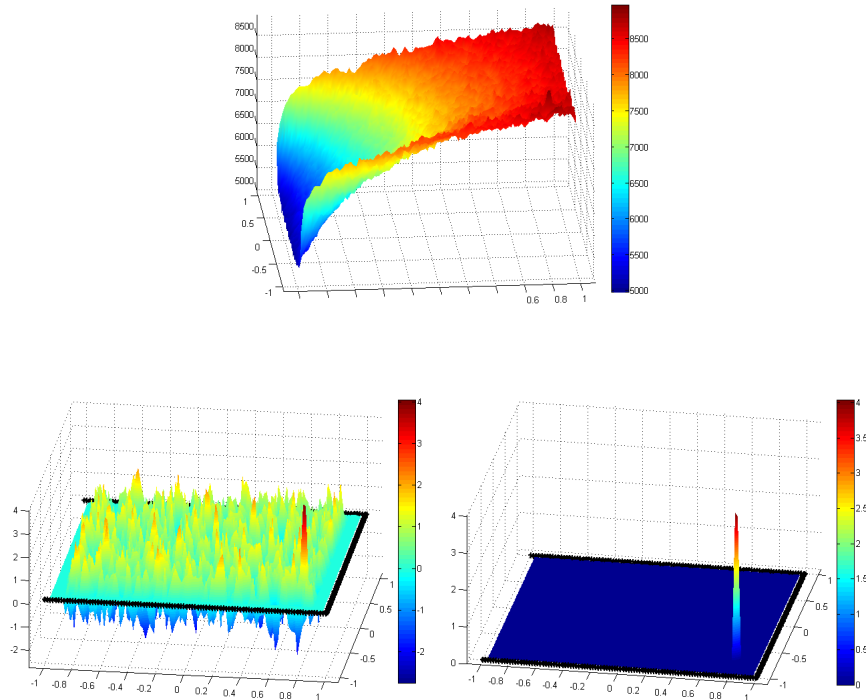


Figure 22: Backprojection reconstruction from Compton data (top). Detected ballistic source particles - 986, background particles - 1,000,002, source location - $(0.803, -0.7041)$. Number of (local) standard deviations above the (local) mean at each pixel is shown on bottom left. The local mean and σ were computed on a 11×11 local grid. Peaks that deviate more than 3.5 (local) standard deviations from the mean are shown on bottom right. Source located at $(0.803, 0.7041)$ is detected with confidence 76.03%.

The source in Fig. 23 is close to the side of the square where there is no detector, which makes it harder to observe. The number of ballistic source particles was 994 versus 10^6 background particles. The local mean and standard deviation were estimated on 7×7 local grids. The confidence level is 96.7%.

Finally, we present an example of a successful detection of several sources (Fig. 24). Three sources were placed inside the imaged area, and three Compton-type detector arrays were used to detect particles. The total number of detected ballistic source particles was 3061, each of the sources having roughly the same contribution. Additional 10^6 random background particles were detected. We have set up the threshold to $k_t = 4.3\sigma$, which gives confidence of detection at least 91.97%. Note that this confidence probability is estimated based on the threshold, and not on the actual number of deviations at each peak, as in the previous examples. Thus, individual confidence probabilities for the three sources discovered are even higher. The local grids we used for estimating the local means and standard deviations had dimensions 11×11 .

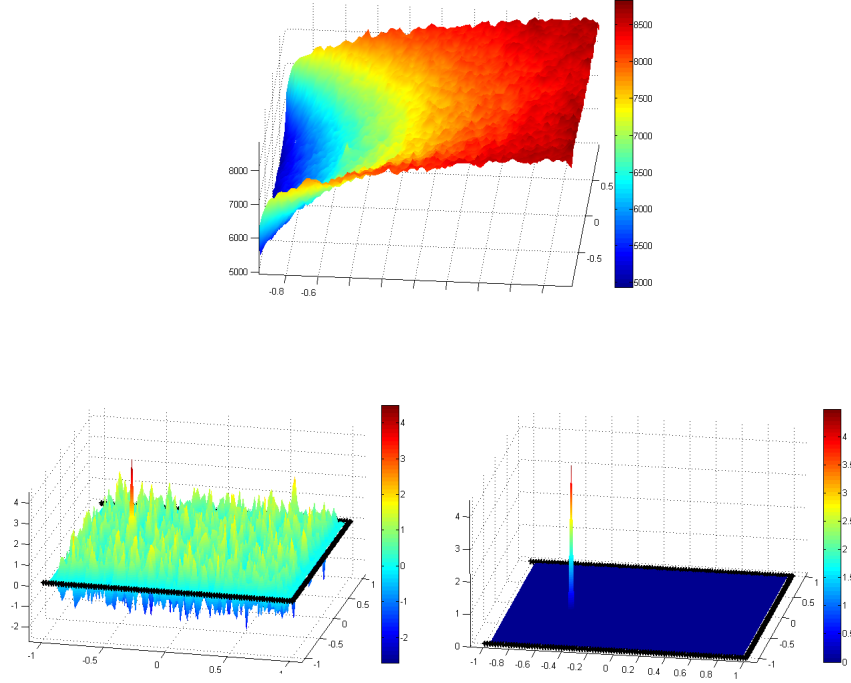


Figure 23: Backprojection reconstruction from Compton data (top). Detected source particles - 994, background particles - 1,000,002, source location - $(-0.503, -0.101)$. Number of (local) standard deviations above the (local) mean at each pixel is shown on bottom left. Peaks that deviate more than 3.5 (local) standard deviations from the mean is shown on bottom right. Source located at $(0.503, 0.101)$ is detected with confidence 96.7%.

8 Final remarks and conclusions

Here are the main conclusions that we have reached:

1. Direction sensitive detectors are needed to be able to uncover existence of a low emission source in the presence of dominating background noise. Collimated cameras, although providing the most valuable direction information, are not applicable, since collimation would decimate the already low signal. Compton type cameras can be used instead.
2. Although standard integral-geometric models of emission tomography (X-ray and Radon transforms and their attenuated versions) are not applicable to the situation of a very weak source, they work to some extent in the detection problem. However, they fail way before the low values of SNR needed in applications.
3. In fact, only the backprojection part of the tomographic reconstruction does the detection work, and the filtering part worsens the results.
4. The (unknown) attenuation might lower the SNR, but otherwise is irrelevant for the validity of the backprojection method.
5. The conclusions above hold both for the collimated and Compton type cameras.

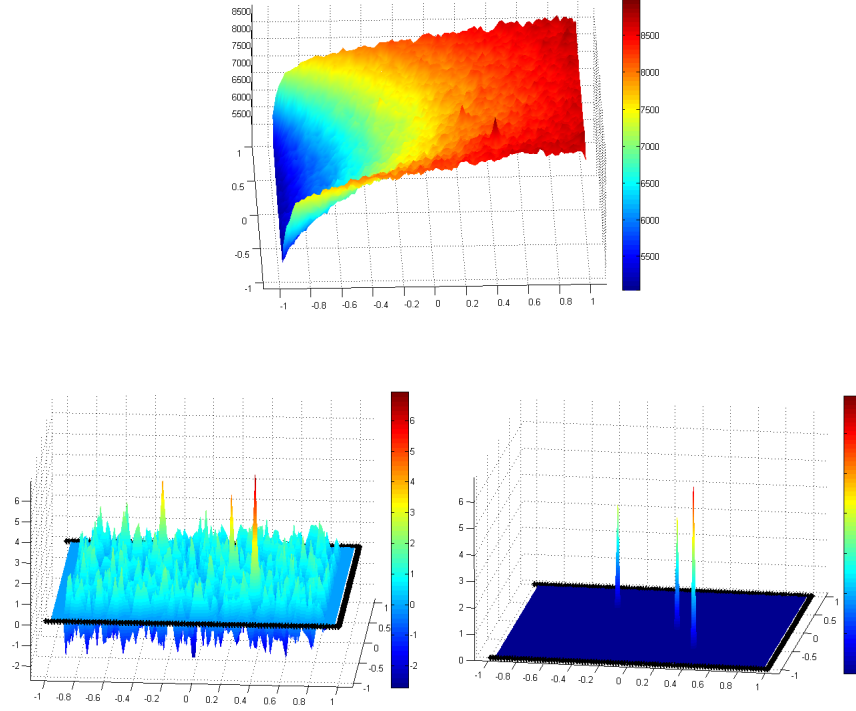


Figure 24: Backprojection reconstruction from Compton data (top). Detected source particles - 3061, background particles - 1,000,002, three sources located at (0.203,-0.101), (-0.301,0.4013) and (0.403,-0.601). Number of (local) standard deviations above the (local) mean at each pixel is shown on bottom left. Peaks that deviate more than 4.3 (local) standard deviations from the mean is shown on bottom right. Confidence of detection based on the threshold $k_t = 4.3$ is 91.97%.

6. The backprojection procedure can be justified by a simple probabilistic consideration, which also provides confidence probabilities of detection.
7. A simple algorithm is provided that recovers the source from Compton data at SNRs on the order 0.1% and beyond. It also provides confidence probabilities. In theoretical considerations and numerical tests, the algorithm demonstrates high sensitivity and specificity. The procedure can be made completely automatic, without the need of a human eye assessment of the image.
8. The algorithm is based upon the assumption of an uniform random background. However, the non-uniformity that arises when the object is only partially surrounded by detector arrays, can be handled successfully by using local grids.

Certainly, there remain quite a few questions that need to be resolved. Some of them will be discussed in the next publication. In particular, 3D Compton backprojection algorithms will be developed and studied analytically and numerically; more complex cargo structures will be modeled and tested, which will involve non-uniform attenuation and scattering; local grid version of the algorithm will be tested on more complex non-uniform random backgrounds than the ones arising due to the partial view; dependence of the results on the precision of Compton type cameras will also be addressed.

As it is done in SPECT, one can try to use Bayesian methods to approach the same detection problem. This was done in 2D case in [45].

Acknowledgments

Work of D. D., G. K., and P. K. was partly supported by the DHS Grant 2008-DN-077-ARI018-04. Work of M. A., D. D., Y. H., and P. K. was partly supported by the NSF DMS grants 0604778 and 0908208. The authors also express their gratitude to W. Charlton, Sunil S. Chirayath, J. Ragusa, and G. Spence for useful discussions and information. Y. H. thanks the Institute for Mathematics and Its Applications (IMA) for the support and hospitality. Research at the IMA is supported by the National Science Foundation and the University of Minnesota.

References

- [1] R. Basko, G. L. Zeng, and G. T. Gullberg, "Application of spherical harmonics to image reconstruction for the Compton camera," *Physics in Medicine and Biology*, vol. 43, pp. 887–894, 1998.
- [2] R. Basko, G. L. Zeng, and G. T. Gullberg, "Analytical reconstruction formula for one-dimensional Compton camera," *IEEE Transactions on Nuclear Science*, vol. 44, no. 3 Part 2, pp. 1342–1346, 1997.
- [3] R. R. Brechner and M. Singh, "Iterative reconstruction of electronically collimated SPECT images," *IEEE Transactions on Nuclear Science*, vol. 37, no. 3 Part 1, pp. 1328–1332, 1990.
- [4] W. Charlton and G. Spence, Private communication, 2009.
- [5] N. H. Clinthorne, C. Y. Ng, C. H. Hua, J. E. Gormley, J. W. Leblanc, S. J. Wilderman, and W. L. Rogers, "Theoretical performance comparison of a Compton-scatter aperture and parallel-hole collimator," in *IEEE Nuclear Science Symposium. Conference Record.*, vol. 2, pp. 788–792, 1996.
- [6] M. J. Cree and P. J. Bones, "Towards direct reconstruction from a gamma camera based on Compton scattering," *IEEE transactions on medical imaging*, vol. 13, no. 2, pp. 398–407, 1994.
- [7] Y. F. Du, Z. He, G. F. Knoll, D. K. Wehe, and W. Li, "Evaluation of a Compton scattering camera using 3-D position sensitive CdZnTe detectors," *Nuclear Instruments and Methods in Physics Research Section A: Accelerators, Spectrometers, Detectors and Associated Equipment*, vol. 457, no. 1-2, pp. 203–211, 2001.
- [8] L. C. Evans, *Partial differential equations*, vol. 19 of *Graduate Studies in Mathematics*. Providence, RI: American Mathematical Society, 1998.
- [9] A. Faridani, E. L. Ritman, and K. T. Smith, Local tomography, *SIAM J. Appl. Math.* **51** (1992), 459–484.
- [10] T. Fawcett, "An introduction to ROC analysis," *Pattern recognition letters*, vol. 27, no. 8, pp. 861–874, 2006.

- [11] I. M. Gelfand and G. E. Shilov, *Generalized functions, part 1 (in Russian)*. Moscow: Gosudarstv. Izdat. Fiz.-Mat. Lit., 1958.
- [12] G. T. Gullberg, G. L. Zeng, and R. Basko, "Image reconstruction from V-projections acquired by Compton camera," Nov. 24 1998. US Patent 5,841,141.
- [13] D. L. Gunter, "*Filtered back-projection algorithm for Compton telescopes*," 2008. US Patent 7,345,283.
- [14] T. Hebert, R. Leahy, and M. Singh, "Three-dimensional maximum-likelihood reconstruction for an electronically collimated single-photon-emission imaging system," *Journal of the Optical Society of America A*, vol. 7, no. 7, pp. 1305–1313, 1990.
- [15] S. Helgason, *The Radon transform*, vol. 5 of *Progress in Mathematics*. Boston, MA: Birkhäuser Boston Inc., second ed., 1999.
- [16] W. H. Hill Jr and K. L. Matthews II, "Experimental verification of a hand held electronically-collimated radiation detector," in *IEEE Nuclear Science Symposium Conference Record, 2007. NSS'07*, vol. 5, pp. 3792–3797,
- [17] Y. Hristova, *Mathematical Problems of Thermoacoustic and Compton Camera Imaging*, PhD Thesis, Texas A&M University, 2010.
- [18] M. Hirasawa and T. Tomitani, "An analytical image reconstruction algorithm to compensate for scattering angle broadening in Compton cameras," *Physics in medicine and biology*, vol. 48, no. 8, pp. 1009–1026, 2003.
- [19] A. C. Kak and M. Slaney, *Principles of Computerized Tomographic Imaging*. IEEE Press, 1988.
- [20] P. Kuchment, "Generalized Transforms of Radon Type and Their Applications," in *The Radon Transform, Inverse Problems, and Tomography* (G. Olafsson and E. T. Quinto, eds.), pp. 67–91, Providence, RI: American Math. Soc., 2006.
- [21] P. Kuchment, K. Lancaster, and L. Mogilevskaya, "On local tomography," *Inverse Problems*, vol. 11, no. 3, pp. 571–589, 1995. 2007.
- [22] A. W. Lackie, K. L. Matthews, B. M. Smith, W. Hill, W. H. Wang, and M. L. Cherry, "A directional algorithm for an electronically-collimated gamma-ray detector," in *IEEE Nuclear Science Symposium Conference Record, 2006*, vol. 1, pp. 264–269, 2006.
- [23] J. W. LeBlanc, N. H. Clinthorne, C. H. Hua, E. Nygard, W. L. Rogers, D. K. Wehe, P. Weilhammer, and S. J. Wilderman, "C-SPRINT: a prototype Compton camera system for low energy gammaray imaging," *IEEE Transactions on Nuclear Science*, vol. 45, no. 3 Part 1, pp. 943–949, 1998.
- [24] C.M. Marianno, D.R. Boyle, W.S. Charlton, and G.M. Gaukler, "A Guide for Detector Development and Deployment," Proceedings of the 2010 Annual Meeting of the Institute of Nuclear Materials Management, Baltimore, MD, July 11-15, 2010.
- [25] V. Maxim, M. Frande, and R. Prost, "Analytical inversion of the compton transform using the full set of available projections," *Inverse Problems*, vol. 25, no. 9, p. 095001, 2009.

- [26] F. Natterer, *The mathematics of computerized tomography*. Philadelphia, PA: Society for Industrial Mathematics, 2001.
- [27] F. Natterer and F. Wübbeling, *Mathematical Methods in Image Reconstruction*. Philadelphia, PA: Society for Industrial Mathematics, 2001.
- [28] M. K. Nguyen, T. T. Truong, and P. Grangeat, "Radon transforms on a class of cones with fixed axis direction," *Journal of Physics A: Mathematical and General*, vol. 38, p. 8003?8015, 2005.
- [29] M. K. Nguyen, T. T. Truong, and P. Grangeat, "Radon transforms on a class of cones with fixed axis direction," *Journal of Physics A: Mathematical and General*, vol. 38, p. 8003, 2005.
- [30] L. C. Parra, "Reconstruction of cone-beam projections from Compton scattered data," *IEEE Transactions on Nuclear Science*, vol. 47, no. 4 Part 2, pp. 1543–1550, 2000.
- [31] R. C. Rohe, M. M. Sharfi, K. A. Kecevar, J. D. Valentine, and C. Bonnerave, "The spatially-variant back-projection point kernel function of an energy-subtraction Compton scatter camera for medical imaging," in *IEEE Nuclear Science*, vol. 2, pp. 2477–2482, 1996.
- [32] G. J. Royle and R. D. Speller, "Compton scatter imaging of a nuclear industry site," in *IEEE Nuclear Science Symposium, 1997*, pp. 365–368, 1997.
- [33] G. J. Royle and R. D. Speller, "A flexible geometry Compton camera for industrial gamma ray imaging," in *IEEE Nuclear Science Symposium. Conference Record.*, vol. 2, pp. 821–824, 1996.
- [34] A. C. Sauve, A. O. Hero III, W. L. Rogers, S. J. Wilderman, and N. H. Clinthorne, "3D image reconstruction for a Compton SPECT camera model," *IEEE Transactions on Nuclear Science*, vol. 46, no. 6, pp. 2075–2084, 1999.
- [35] M. Singh, "An electronically collimated gamma camera for single photon emission computed tomography. Part I: Theoretical considerations and design criteria," *Medical Physics*, vol. 10, pp. 421–427, 1983.
- [36] M. Singh and D. Doria, "An electronically collimated gamma camera for single photon emission computed tomography. Part II: Image reconstruction and preliminary experimental measurements," *Medical Physics*, vol. 10, pp. 428–435, 1983.
- [37] V. Schönfelder, H. Aarts, K. Bennett, H. De Boer, J. Clear, W. Collmar, A. Connors, A. Deerenberg, R. Diehl, A. von Dordrecht, *et al.*, "Instrument description and performance of the imaging gamma-ray telescope COMPTEL aboard the Compton Gamma-Ray Observatory," *Astrophysical Journal*, vol. 409, pp. 492–492, 1993.
- [38] B. Smith, "Reconstruction methods and completeness conditions for two Compton data models," *Journal of the Optical Society of America A*, vol. 22, no. 3, pp. 445–459, 2005.
- [39] G.R. Spence and W.S. Charlton, "Directionally Sensitive Neutron Detectors for Portal Monitors," Proceedings of the 2009 Annual Meeting of the Institute of Nuclear Materials Management, Tucson, AZ, July 12-15, 2009.
- [40] R. W. Todd, J. M. Nightingale, and D. B. Everett, "A proposed gamma camera," *Nature*, vol. 251, pp. 132–134, 1974.

- [41] T. Tomitani and M. Hirasawa, “Image reconstruction from limited angle Compton camera data,” *Physics in Medicine and Biology*, vol. 47, pp. 2129–2145, 2002.
- [42] T. T. Truong, M. K. Nguyen, and H. Zaidi, “The mathematical foundations of 3D Compton scatter emission imaging,” *International Journal of Biomedical Imaging*, vol. 2007, 2007.
- [43] S. Watanabe, T. Tanaka, K. Nakazawa, T. Mitani, K. Oonuki, T. Takahashi, T. Takashima, H. Tajima, Y. Fukazawa, M. Nomachi, *et al.*, “A Si/CdTe Semiconductor Compton Camera,” *IEEE Transactions on Nuclear Science*, vol. 52, no. 5 Part 3, pp. 2045–2051, 2005.
- [44] S. Wilderman, W. L. Rogers, G. F. Knoll, and J. C. Engdahl, “Fast algorithm for list mode back-projection of Compton scatter camera data,” *IEEE Transactions on Nuclear Science*, vol. 45, no. 3 Part 1, pp. 957–962, 1998.
- [45] X. Xun, B. Mallick, R. Carroll, P. Kuchment, A Bayesian Approach to Detection of Small Low Emission Sources, preprint 2010.